Local thermal externalities of hyperscale datacenters: causal satellite evidence and implied cooling costs

Jorge Colazo
Associate Professor of Business Analytics
Department of Finance and Business Analytics
Trinity University
One Trinity Place, San Antonio, TX 78212, United States
Email: jcolazo@trinity.edu | Phone: 210-999-7287
ORCID: 0000-0003-1636-6923

This is a non-peer reviewed pre print. The paper is currently under review at Energy Economics.

Abstract

Hyperscale datacenter construction converts agricultural or greenfield land into continuous heat rejection campuses, yet no causal estimate of the resulting local thermal effect exists. This paper applies a Callaway and Sant'Anna (2021) staggered difference-in-differences estimator to spatially differenced Landsat satellite thermal imagery across 59 datacenter sites in the United States, with treatment onset dated independently of the thermal outcome using Visible Infrared Imaging Radiometer Suite (VIIRS) nighttime radiance. The VIIRS dating is validated against 17 independently documented commissioning dates (median absolute error of one month; 94 percent within three months). The estimated change in the daytime land-surface temperature (LST) gradient relative to the 5 to 10 km reference ring following energization peaks at +0.80 K in the 500 m to 1 km band (significant at 1 percent), with +0.38 K within 500 m (SE = 0.19, significant at 10 percent) and +0.24 K at 2 to 5 km. The sign is stable across leave-one-cohort-out specifications and seasonal subsamples, although magnitude and precision vary, and the estimate strengthens when datacenter cluster markets are excluded. Translating the thermal gradient into implied annual residential cooling expenditures under alternative persistence and LST-to-air conversion assumptions produces a sample-wide central estimate of $0.50 million per year across 46 operational sites, with joint scenario bounds between $0.17 and $0.88 million. This is a detectable but modest channel relative to facility scale, equivalent to roughly $52 per megawatt-year in the subsample with documented capacity.

JEL classification: H23, Q51, Q54, R14

Keywords: externalities; datacenters; land-surface temperature; staggered difference-in-differences; cooling costs; infrastructure siting

1. Introduction

The global buildout of hyperscale datacenter infrastructure represents one of the largest capital investment waves in recent decades. In the United States alone, 155 projects totaling $276 billion were announced during 2024, with cumulative planned capacity exceeding 45 gigawatts (Synergy Research Group 2025). Each facility converts agricultural or greenfield land into a continuous heat rejection campus, dissipating 20 to 500 megawatts (MW) of heat through cooling towers and exhaust systems while replacing vegetated surfaces with impervious cover (Shehabi et al. 2016; Masanet et al. 2020). The scale is substantial: the International Energy Agency (IEA) (2024) projects global datacenter electricity consumption to exceed 1,000 TWh by 2026, roughly equivalent to Japan's total electricity demand. Forecasting work anticipates that usage growth will outpace efficiency gains, ending the earlier era of roughly flat datacenter electricity consumption (Koot and Wijnhoven 2021), and the deployment of generative artificial intelligence adds server capacity whose electricity demand alone could rival that of a mid-sized country (de Vries 2023). Where this capacity locates is an economic decision: hyperscale operators trade off land costs, power availability, and tax incentives toward peripheral and exurban sites (Fang and Greenstein 2025; Depoorter et al. 2015), which places large heat rejection campuses near communities that previously hosted agriculture or low-density development.

The local consequences of hosting such facilities are the subject of a growing empirical literature. County-level evidence finds that datacenter expansion raises local employment, wages, tax revenue, and housing prices, but also electricity costs (Alvarez et al. 2026). A long tradition in environmental economics shows that the costs of proximate industrial and energy facilities are capitalized into housing markets, from hazardous waste sites (Greenstone and Gallagher 2008) and shale gas wells (Muehlenbachs et al. 2015) to wind turbines (Gibbons 2015; Droes and Koster 2016), and that local opposition to energy infrastructure carries measurable social costs (Jarvis 2025). Datacenters fit this template of spatially concentrated costs and diffuse benefits, but the thermal channel specific to them has not been measured causally.

Community opposition to datacenter siting has intensified. In Virginia's Loudoun County, the largest datacenter market in the world, county supervisors imposed a 2024 moratorium on new applications after resident complaints about noise, water consumption, and perceived heat effects (Loudoun County Board of Supervisors 2024). Similar moratoriums or restrictive zoning actions have been enacted in Dublin (An Bord Pleanala 2022), Singapore (Infocomm Media Development Authority 2019), and multiple US jurisdictions. Across 2024 and 2025, 64 datacenter projects representing $64 billion in investment were blocked or delayed by local opposition (Synergy Research Group 2025). Yet the siting debate proceeds almost entirely without causal empirical evidence on the magnitude of local thermal externalities. The evidentiary gap matters in both directions: if thermal effects are large, current zoning treats affected households inequitably; if they are small, moratoria justified on thermal grounds forgo local employment and tax gains and push capacity toward jurisdictions with weaker review, at the social costs documented for opposition to other energy infrastructure. Distinguishing the two cases requires an estimate that separates the effect of the facility from the characteristics of the places where facilities locate.

Recent descriptive studies have begun to document elevated surface temperatures near datacenter sites. Marinoni et al. (2026) report global mean warming of +2.07 K within 100 m of 4,000 facilities using Landsat data, and Chakraborty et al. (2026) find +1.44 K summer effects at approximately 10,000 sites, attributing the signal primarily to vegetation loss. Jing (2026) separates thermal channels in Japan using multi-sensor analysis, finding daytime warming from albedo change but no detectable nighttime waste heat signal. Sailor et al. (2026) provide the only field measurements, documenting 0.7 to 2.2 °C air-temperature increases within 500 m of a single campus in Portland, Oregon, but lack a credible counterfactual for causal inference. These studies establish the spatial pattern of elevated temperatures near datacenters but cannot attribute the thermal effect to datacenter development specifically, because sites are selected on pre-existing land-use and climate characteristics that also affect local temperature.

The causal identification challenge is twofold. First, datacenter operators select sites in locations with specific thermal, topographic, and regulatory characteristics (cheap land, low humidity, proximity to power substations), creating systematic site-selection bias that inflates cross-sectional thermal correlations. Second, dating treatment onset from the outcome variable itself (identifying when a temperature jump occurs in the thermal record) mechanically biases difference-in-differences (DiD) estimates upward (Roth 2022). Addressing both problems simultaneously requires panel variation in treatment timing identified from a source external to the outcome.

This paper addresses the causal identification gap. The empirical setting is the United States hyperscale fleet between 2015 and 2025, a period spanning the cloud-computing expansion and the first wave of artificial intelligence training campuses. The United States hosts the largest concentration of hyperscale capacity in the world and some of the most active siting disputes. Because most of the fleet was energized within the Landsat 8 and 9 observation window, its rollout pattern is suitable for panel identification: facilities entered operation in staggered cohorts spread across nine years, in locations determined by land, power, fiber, and tax considerations rather than by local climate trajectories. A Callaway and Sant'Anna (2021) staggered DiD estimator is applied to spatially differenced Landsat satellite thermal imagery across 59 hyperscale datacenter sites. Treatment onset is dated independently of the thermal outcome using Visible Infrared Imaging Radiometer Suite (VIIRS) nighttime radiance, which detects facility energization through a distinct satellite sensor operating at a different wavelength and spatial scale than Landsat thermal infrared. Spatial differencing (subtracting each site's 5 to 10 km reference ring temperature from its near-field temperature) removes common weather variation, isolating near-field warming from background climate trends. The daytime LST change is then translated into implied residential cooling expenditures using site-level population counts from the Global Human Settlement Layer (GHSL) and state-level residential electricity rates.

The analysis produces three main findings. First, facility energization detectably warms the near-field surface relative to the surrounding reference ring, with the effect largest just beyond the campus boundary and declining with distance; the spatial and seasonal pattern is more consistent with land-cover change than with waste heat alone. Second, the causal estimate is substantially smaller than the correlational magnitudes reported in cross-sectional studies, consistent with site-selection confounding inflating descriptive comparisons. Third, the implied household cooling burden is small when set against the scale of the facilities themselves, and it falls almost entirely on the handful of sites bordering dense housing, an incidence pattern that favors targeted mitigation over broad siting restrictions.

This paper contributes to the literature in four ways. First, it provides the first causal estimate of the daytime surface-temperature change following datacenter energization, using quasi-experimental variation from staggered treatment timing to address the site-selection confounding inherent in prior cross-sectional studies. Second, the external treatment dating strategy resolves the endogenous-dating bias that arises when treatment onset is detected from the outcome variable, using an independent satellite sensor (VIIRS nighttime radiance) that measures a physically distinct quantity from Landsat thermal infrared. Third, the spatially differenced outcome design (inner band minus reference ring) removes common weather variation within site-months, sharpening precision relative to level-on-level comparisons. Fourth, the paper introduces a site-level implied-cost framework with bootstrapped uncertainty propagation that translates physical temperature estimates into residential cooling expenditures, providing a direct input for benefit-cost analysis of proposed facilities.

The paper proceeds as follows. Section 2 reviews the related literature. Section 3 describes the data sources and sample construction. Section 4 presents the identification strategy and estimation approach. Section 5 reports the thermal and economic impact results. Section 6 examines robustness to alternative specifications. Section 7 discusses implications and limitations.

2. Literature review

This paper draws on three strands of literature: the urban heat island (UHI) and infrastructure thermal effects literature, the emerging literature on datacenter environmental impacts, and the econometric literature on staggered DiD estimation.

2.1. Urban heat islands and infrastructure thermal effects

The relationship between land-use change and local temperature is well established. Oke (1982) first formalized the energy balance framework linking impervious surface cover to urban heat islands, and subsequent work has refined the mechanisms: reduced evapotranspiration from vegetation removal, decreased albedo from dark surfaces, and anthropogenic waste heat release (Arnfield 2003; Stewart and Oke 2012; Oke et al. 2017). Remote sensing studies using Landsat and Moderate Resolution Imaging Spectroradiometer (MODIS) satellites have documented UHI effects ranging from 1 to 8 K across cities, with magnitude depending on city size, climate zone, and land-cover composition (Imhoff et al. 2010; Zhou et al. 2014; Clinton and Gong 2013; Peng et al. 2012). The measurement basis for this literature is well characterized: Voogt and Oke (2003) set out how satellite-observed surface temperature relates to, and differs from, the air-temperature heat island, and the operational retrieval algorithms behind the MODIS and Landsat LST products have been validated to accuracies of roughly 1 to 2 K (Wan 2014; Malakar et al. 2018), including the single-channel retrieval underlying the Landsat Collection 2 surface temperature product used here.

The economics of urban heat is increasingly quantified. Estrada et al. (2017) estimate that the urban heat island roughly doubles the local cost of climate change for a global sample of cities, and that cool-surface mitigation policies pass benefit-cost tests. Each degree of ambient warming raises building cooling electricity demand by roughly 0.5 to 8.5 percent across empirical studies (Santamouris et al. 2015), warming raises peak as well as average electricity load (Auffhammer et al. 2017), and classic estimates value UHI mitigation through cool surfaces and shade trees in the billions of dollars annually for the United States (Akbari et al. 2001).

Infrastructure-specific thermal externalities have received less attention. Power plant cooling systems produce localized thermal plumes (Madden et al. 2013), and Li et al. (2013) document that industrial land-use conversion raises local surface temperatures through the same mechanisms as urban expansion. The economic consequences of localized heating include increased residential cooling demand (Deschenes and Greenstone 2011; Auffhammer and

Mansur 2014; Davis and Gertler 2015; Barreca et al. 2016), property value depreciation near heat-emitting facilities (Davis 2011), and health effects from heat exposure (Deschenes and Moretti 2009; Carleton et al. 2022).

2.2. Datacenter environmental impacts

The datacenter environmental literature has developed rapidly, driven by the exponential growth in computational demand from cloud computing and artificial intelligence training (Masanet et al. 2020; Patterson et al. 2021). Research has focused on three channels of environmental impact: electricity consumption and associated emissions (Lei and Masanet 2020; IEA 2024; Mytton 2021), water consumption for evaporative cooling (Shehabi et al. 2016; Ristic et al. 2015), and local environmental externalities including noise and thermal effects (Muller 2026). Facility-level accounting shows that the water footprint of US datacenters is dominated by indirect use through electricity generation and that facilities are frequently sited in water-stressed basins (Siddik et al. 2021), while the spatial flexibility of computational load allows facilities to interact with the grid, absorbing renewable curtailment through load migration between sites (Zheng et al. 2020).

Muller (2026) provides a comprehensive economic valuation of datacenter air pollution and greenhouse gas externalities using the AP3 model, estimating annual damages of $18 billion in the United States. However, thermal externalities are absent from that accounting framework, partly because no causal estimates existed. Sailor et al. (2026) document the first field measurements of datacenter thermal impacts, deploying weather stations near a Portland campus and finding air-temperature elevations of 0.7 to 2.2 °C, but the single-site design precludes generalization and the absence of a counterfactual (pre-construction baseline or matched control) prevents causal attribution.

Three concurrent satellite studies examine datacenter thermal footprints at scale. Marinoni et al. (2026) use a global cross-section of 4,000 sites, measuring LST within distance bands and reporting mean warming of +2.07 K at 100 m. Their design relies on spatial differencing against a far ring but does not exploit temporal variation in site construction, leaving the estimate vulnerable to site-selection confounding: locations chosen for datacenter development may have been warmer than their surroundings before construction. Chakraborty et al. (2026) analyze approximately 10,000 datacenter locations in the United States, finding a +1.44 K summer effect and attributing the signal primarily to vegetation loss through fractional vegetation cover analysis. Their design also lacks temporal variation and relies on spatial comparisons between datacenter pixels and matched control pixels selected on observable covariates. Jing (2026) provides the most mechanistically detailed analysis, using multi-source satellite observations in Japan to separate thermal channels: daytime warming from albedo and land-cover change is clearly detected, but nighttime thermal signals attributable to waste heat are indistinguishable from zero. This finding has important implications for mechanism interpretation: if daytime thermal effects primarily reflect land-cover change rather than waste heat, then mitigation strategies should target site design and vegetation rather than cooling system engineering.

The present study extends this literature by exploiting the staggered timing of datacenter energization as a source of identification. The resulting causal estimate can be compared directly to these cross-sectional magnitudes.

2.3. Staggered difference-in-differences

Recent advances in DiD methodology have demonstrated that standard two-way fixed effects (TWFE) estimators produce biased estimates when treatment effects are heterogeneous across cohorts and over time (de Chaisemartin and D'Haultfoeuille 2020; Goodman-Bacon 2021; Sun and Abraham 2021; Borusyak et al. 2024). The bias arises because TWFE implicitly uses already-treated units as controls for later-treated units, contaminating the comparison when treatment effects change over time. Several heterogeneity-robust estimators have been proposed. Callaway and Sant'Anna (2021) estimate group-time average treatment effects ATT(g,t) for each cohort g and calendar period t, then aggregate using transparent weighting schemes. Sun and Abraham (2021) implement an interaction-weighted estimator within the TWFE regression framework. Borusyak et al. (2024) develop an imputation estimator that directly constructs counterfactual outcomes for treated units.

The choice of control group is a first-order design decision (Callaway and Sant'Anna 2021; Baker et al. 2022; Roth et al. 2023). Using never-treated units as controls is valid only if the never-treated group is comparable to the treated group on unobservables, a strong assumption in settings where treatment eventually reaches all eligible units. Not-yet-treated controls, used in the present study, relax this assumption by comparing each treated cohort against units that will be treated in the future but have not yet been treated at the comparison date. This requires that the exact timing of treatment is unrelated to potential outcomes conditional on observables, an assumption that cannot be verified directly. External dating removes one specific threat: because VIIRS nighttime radiance captures the physical event of facility energization rather than a break detected in the outcome series, the mechanical dating bias described by Roth (2022) is ruled out. Timing exogeneity beyond that rests on the observation that the staggered rollout across sites reflects idiosyncratic construction and commissioning timelines, and is probed through the pre-trend diagnostics in Sections 5 and 6.

Two further strands of this literature shape the empirical practice adopted here. On pre-trend assessment, Freyaldenhoven et al. (2019) show how confound-driven pre-event trends bias panel event studies, and Rambachan and Roth (2023) develop sensitivity analysis for bounded violations of parallel trends, motivating the reporting of multiple pre-treatment diagnostics rather than a single test; event-study paths are displayed with simultaneous sup-t bands following Montiel Olea and Plagborg-Moller (2019), since pointwise intervals understate joint uncertainty across event-time coefficients. On inference, a small number of treated units renders standard cluster-asymptotic inference unreliable (Conley and Taber 2011; Ferman and Pinto 2019; Cameron et al. 2008), a consideration that applies directly to the 46-site treated sample and motivates the conservative reading of marginal significance levels adopted throughout.

Donaldson and Storeygard (2016) review the use of remote sensing in economics, emphasizing the potential for satellite data to provide outcome measures that are immune to reporting biases and available at fine spatial resolution. Henderson et al. (2012) pioneer the use of nighttime lights as economic proxies. Marx et al. (2019) use satellite-derived roof-quality measures to study housing investment in informal settlements. The present study contributes to this tradition by using two satellite systems for distinct purposes: Landsat for the outcome (thermal imagery) and VIIRS for the treatment (nighttime radiance as a proxy for operational status), exploiting the physical independence of the two measurements.

3. Data

3.1. Site panel construction

The site panel merges four publicly available datacenter location databases: the Kollar and Grady (2025) Zenodo repository, the IM3 Data Center Atlas from Pacific Northwest

National Laboratory (O'Neill et al. 2022), the Epoch AI Frontier Data Centers dataset (Epoch AI 2025), and Meta public disclosures. The four sources have complementary coverage: the Zenodo repository provides the broadest facility census, the IM3 Atlas contributes engineering attributes, the Epoch AI dataset tracks the largest artificial-intelligence training campuses with capacity estimates, and operator disclosures pin coordinates for facilities that third-party databases geocode imprecisely. Merging mitigates the selective coverage any single source would impose on the sample. Spatial deduplication at a 2 km threshold produces 1,109 unique site clusters, of which 262 are classified as hyperscale (exceeding 20 MW or 100,000 square feet). Figure 1 maps the site locations by treatment status.

3.2. Satellite data sources

Land-surface temperature (LST) is extracted from Landsat 8 and 9 Collection 2 Level 2 science products through Google Earth Engine at 30 m delivered grid (100 m native thermal resolution, resampled by the United States Geological Survey (USGS)), covering January 2015 through December 2025. For each site-month, median LST is computed within five concentric distance bands centered on the site coordinates: 0 to 500 m (b0), 500 m to 1 km (b1), 1 to 2 km (b2), 2 to 5 km (b3), and 5 to 10 km (b4). Two wider rings, 10 to 20 km (b5) and 20 to 30 km (b6), are additionally extracted at 200 m scale for the reference-ring checks in Section 6.6. Landsat thermal infrared provides daytime surface temperature at each overpass (approximately every 16 days per satellite), and monthly medians reduce cloud contamination and orbital sampling artifacts. Observations with any band-level LST below 230 K are excluded as residual cloud contamination, affecting less than 0.5% of site-months.

VIIRS Day/Night Band monthly composites from the National Oceanic and Atmospheric Administration (NOAA) at 500 m resolution provide the independent treatment indicator. VIIRS data are available from April 2012, predating the Landsat panel start by approximately three years, which allows assessment of pre-existing operational status. The VIIRS nighttime radiance signal responds to the electrification and illumination of datacenter campuses, which is physically distinct from the Landsat thermal infrared signal that responds to surface and near-surface temperature.

3.3. Population and economic data

Population exposure is measured from the Joint Research Centre (JRC) Global Human Settlement Layer (GHSL) at 100 m resolution (2023 release), summing population within each distance band and converting to households at 2.53 persons per household (US Census Bureau 2020). State-level residential electricity rates are from the US Energy Information Administration (EIA) (2024), used to convert cooling energy demand into dollar-valued expenditures. Table 1 reports descriptive statistics for the analysis sample.

3.4. Sample construction

The analysis sample is constructed through two exclusion steps. First, 187 sites that were already operational when VIIRS launched (initial 12-month mean radiance exceeding the detection threshold) are excluded, because they cannot be externally dated and would contaminate the control group as always-treated units. Second, 16 sites with detected treatment onset before January 2016 are excluded entirely: the Landsat panel (starting January 2015) provides insufficient pre-treatment observations to estimate their treatment effects, and because these facilities are already operational throughout the usable outcome window, they are not valid untreated controls either. The retained sample comprises 59 sites: 46 treated sites with externally dated onset across 9 annual cohorts (2016 to 2025), plus 13 not-yet-treated or never-treated control sites (Table 2). The small control group is a direct consequence of the strict exclusion rules; the Callaway and Sant'Anna estimator additionally uses later-treated cohorts as not-yet-treated controls for earlier cohorts, so the effective comparison group at each date is larger than the 13 never-treated sites alone.

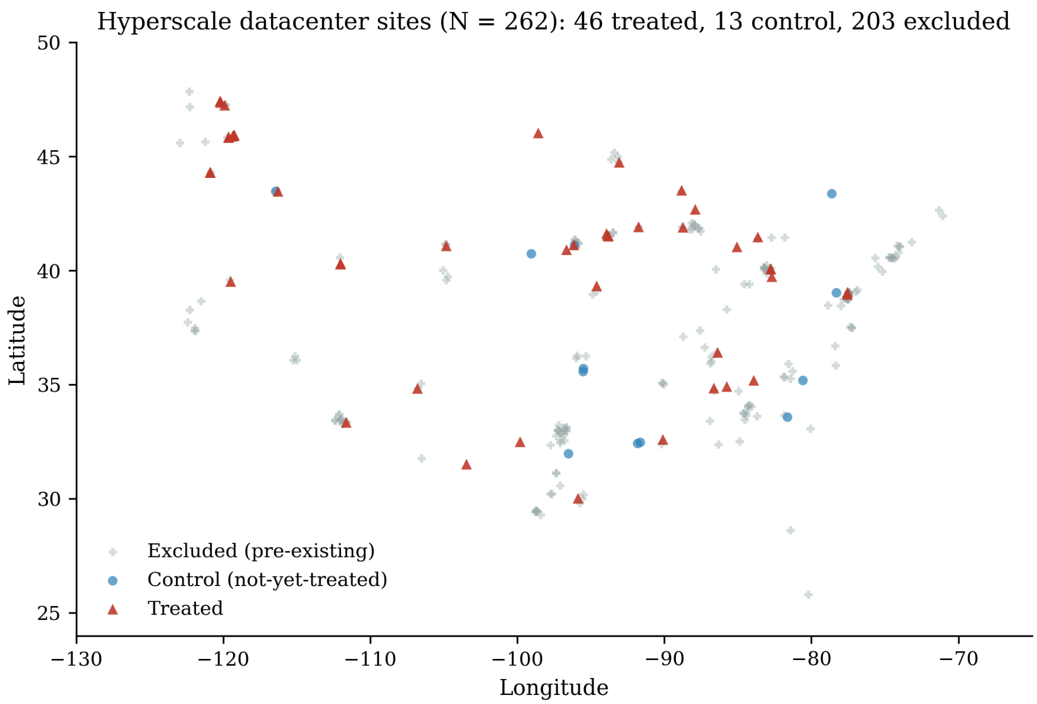

Figure 1. Hyperscale datacenter sites by treatment status. Triangles: treated (n = 46); circles: control (n = 13); crosses: excluded pre-existing (n = 187).

Table 1. Descriptive statistics.

Variable	Mean	SD	Min	Max	N
LST 0-500 m (K)	290.4	18.3	230.2	337.8	35,058
LST 500 m-1 km (K)	290.2	18.0	230.9	337.8	35,068
LST 1-2 km (K)	289.9	17.8	230.2	336.8	35,093
LST 2-5 km (K)	289.7	17.4	230.1	336.4	35,147
LST 5-10 km (ref) (K)	289.3	17.1	230.2	336.0	35,229

Households 0-500 m	12	51	0	349	46
Households 500 m-1 km	47	197	0	1343	46
Households 1-2 km	235	343	0	1291	46
Households 2-5 km	3772	4725	0	23143	46
Power capacity (MW)	97.2	118.8	0	369	15

Notes: LST in Kelvin from Landsat 8/9 monthly medians. Households from GHSL 2023 at 2.53 persons/household. Power capacity reported for sites with any database entry; zero-valued entries are missing-data placeholders and are treated as missing in the per-MW analysis (Section 5.3).

Table 2. Sample composition by treatment cohort.

Cohort year	Sites
2016	6
2017	6
2018	4
2019	3
2020	5
2021	4
2022	4
2024	7
2025	7
Control (never/not-yet-treated)	13
Total retained	59

Notes: Treatment onset dated from VIIRS nighttime radiance threshold crossing. 187 pre-existing sites and 16 early cohort sites excluded (treated before the usable Landsat pre-period). No site crossed the detection threshold during 2023.

4. Identification strategy and estimation

4.1. External treatment dating

A central methodological concern in satellite-based DiD studies of infrastructure impacts is endogenous treatment dating: if treatment onset is detected from the outcome variable (for example, by applying structural break detection to the LST time series), the detected break date mechanically coincides with a large positive realization in the outcome, biasing DiD estimates upward (Roth 2022).

Treatment onset is instead dated from an independent satellite sensor: NOAA VIIRS Day/Night Band monthly composites. A site is classified as operational in the first month its mean nighttime radiance exceeds 5 nW/cm²/sr for six or more consecutive months, provided that its initial 12-month baseline radiance is below this threshold. The 5 nW/cm²/sr threshold is selected on dating accuracy against documented commissioning dates (Section 4.2), independent of the thermal results; it exceeds typical rural ambient radiance (generally below 2 nW/cm²/sr) while remaining below the radiance produced by datacenter campus illumination and parking area lighting (typically 10 to 50 nW/cm²/sr at 500 m resolution). The six-month sustain requirement filters transient agricultural or construction lighting. Sensitivity of the thermal estimates to the threshold is examined in Section 6.

The independence of the treatment indicator rests on the physical separation between VIIRS nighttime radiance (visible/near-infrared wavelengths, responding to artificial lighting) and Landsat thermal infrared (10.6 to 12.5 μm, responding to surface emitted radiation). A facility that becomes operational generates nighttime light emissions (detected by VIIRS) and thermal emissions (detected by Landsat), but these are recorded by different sensors at different wavelengths, times of day, and spatial resolutions, eliminating mechanical correlation between the treatment indicator and the outcome measurement error.

4.2. Validation against documented commissioning dates

The dating procedure is validated against 17 facilities whose commissioning dates are documented in operator disclosures, sustainability reports, and local press records, compiled independently of the satellite data. Table 3 reports the validation results for each candidate threshold: the number of documented facilities the procedure can date, the count it fails to date (classified pre-existing or never crossing the threshold), and the count it dates more than six months before the documented commissioning (premature detection). The table also reports the mean absolute error (MAE) of the dating and the share of dated facilities within three and six months of the documented date.

At the baseline 5 nW/cm²/sr threshold, all 17 documented facilities are dated, with a mean absolute error of 0.9 months, a median absolute error of one month, 94 percent within three months, and 100 percent within six months, with no premature detections. Accuracy deteriorates sharply in both directions. At 3 nW/cm²/sr, six documented facilities become undatable (ambient radiance is classified as pre-existing operation) and seven are dated prematurely, because rural background radiance crosses the lower threshold before energization. At 7 and 10 nW/cm²/sr, all facilities are dated but with mean absolute errors of 14.5 and 26.7 months, because campus radiance takes months or years after energization to accumulate past the higher thresholds. The validation therefore fixes the 5 nW/cm²/sr threshold on dating accuracy grounds before the thermal estimates are examined, and simultaneously explains the pattern of threshold sensitivity in Section 6.1: alternative thresholds produce different thermal estimates primarily because they misdate treatment, not because the underlying thermal signal is fragile.

4.3. Spatial differencing

The outcome variable is constructed as the spatially differenced LST: for each site-month, the temperature in each inner distance band (b0 through b3) is subtracted from the temperature in the 5 to 10 km reference ring (b4). This spatial differencing removes common weather variation, local climate trends, and sensor calibration artifacts that affect all distance bands equally within a site-month, isolating near-field warming relative to the surrounding landscape. The differenced outcome is then de-seasonalized by subtracting site × band × calendar-month means computed from pretreatment observations only, removing systematic seasonal patterns in the inner-minus-outer temperature gradient.

4.4. Callaway and Sant'Anna estimation

Standard TWFE estimators produce biased estimates under treatment effect heterogeneity across cohorts and time (de Chaisemartin and D'Haultfoeuille 2020; Goodman-Bacon 2021). The estimator therefore follows Callaway and Sant'Anna (2021). For each cohort g (sites sharing a VIIRS-dated treatment month) and calendar period t, a group-time ATT(g,t) is estimated through a 2 × 2 DiD comparing the change in de-seasonalized, spatially differenced LST for cohort g between the base period (one month before g) and period t, against the same change for not-yet-treated controls.

The control group consists of sites whose VIIRS-dated treatment month is strictly later than the comparison period t, or sites that are never treated during the sample window. This not-yet-treated control group avoids the contamination problems of already-treated controls documented by Goodman-Bacon (2021) and Borusyak et al. (2024).

Group-time effects are aggregated into three summary measures: (i) an overall post-treatment ATT, weighted by cohort size; (ii) an event study by relative time, pooling across cohorts at each month relative to treatment; and (iii) distance-band estimates for the spatial decay analysis. Aggregate standard errors are computed using the variance formula for weighted averages. Standard errors at the group-time level combine within-group and within-control-group variation and are clustered at the site level.

Table 3. Validation of VIIRS treatment dating against independently documented commissioning dates, by candidate detection threshold.

Threshold (nW/cm²/sr)	Facilities dated	Undetected	Premature	MAE (months)	Within 3 months	Within 6 months
3	11 of 17	6	7	17.0	36%	36%
5	17 of 17	0	0	0.9	94%	100%
7	17 of 17	0	0	14.5	59%	59%
10	17 of 17	0	0	26.7	29%	29%

Notes: Validation sample: 17 facilities with commissioning dates documented in operator disclosures, sustainability reports, and local press records, compiled independently of the satellite data. Undetected: documented facility the procedure cannot date (classified pre-existing or no sustained radiance crossing). Premature: VIIRS date more than 6 months before the documented commissioning date. MAE: mean absolute dating error among dated facilities. The validation is computed on all panel sites before sample exclusions.

5. Results

5.1. Main thermal effect

Table 4 reports the Callaway and Sant'Anna estimates. Panel A presents the main results. The overall post-treatment ATT on spatially differenced LST within the 0 to 500 m band is +0.38 K (SE = 0.19, t = 1.93, 95% CI [-0.01, 0.76]), significant at the 10 percent level, with the 95 percent confidence interval marginally including zero. As Section 5.2 shows, the strongest and most precisely estimated effects appear in the 500 m to 1 km and 1 to 2 km bands rather than in the facility footprint band itself.

Three pre-treatment diagnostics are reported. The aggregated pre-treatment ATT is -0.25 K ($t = -1.09$), failing to reject parallel trends. A linear trend fitted to the pre-treatment event-study coefficients has a slope of 0.0066 K per month ($p = 0.77$), showing no systematic drift in the inner-versus-outer gradient before energization. A joint Wald test across all pre-treatment group-time cells rejects the null of exactly zero pre-treatment effects ($p < 0.001$); with 275 degrees of freedom and monthly cells, this test picks up scattered non-systematic deviations in individual cohort-month cells rather than a common pre-trend, which is the threat to identification. The absence of an aggregate pre-treatment effect and of a systematic slope is the relevant evidence for the design, but the joint rejection is reported for completeness.

Figure 2 displays the event study with both pointwise and simultaneous (sup-t) 95 percent bands. Pre-treatment coefficients fluctuate around zero with no systematic trend, supporting the parallel trends assumption, although the month-to-month coefficients are noisy and the visual break at energization is gradual rather than sharp. Post-treatment coefficients turn positive within the first few months and grow over time: the long-run ATT (months 12 to 24) is +0.55 K, with 10 of 13 coefficients positive. The gradual build-up is consistent with facilities ramping to full operational capacity over the first year, as cooling loads scale with computational demand during phased commissioning.

5.2. Spatial decay

Panel B of Table 4 and Figure 3 report the ATT by distance band. The thermal effect is not monotonically declining: the 500 m to 1 km band (+0.80 K) shows a larger effect than the 0 to 500 m band (+0.38 K), followed by a decline to +0.58 K at 1 to 2 km and +0.24 K at 2 to 5 km. The 500 m to 1 km and 1 to 2 km bands are significant at the 1 percent level and the 2 to 5 km band at the 5 percent level, while the 0 to 500 m band is significant at the 10 percent level only.

The non-monotonic pattern, with b1 exceeding b0, is consistent with the 0 to 500 m ring including the facility footprint itself, where building thermal properties (high thermal mass, reflective roofing in some facilities) differ from the heat plume diffusing into surrounding disturbed land. The b1 ring (500 m to 1 km) captures the zone of maximum impact: immediately beyond the campus boundary, where waste heat from cooling towers combines with land-cover disruption from construction, parking, and access roads. Beyond 1 km, the effect attenuates as the thermal plume disperses and the landscape returns to its pre-construction state.

The only available field measurements fall just inside the zone where the satellite gradient peaks. Sailor et al. (2026) record air-temperature elevations of 0.7 to 2.2 °C within roughly 500 m of a single Portland campus; measured from the campus fence line rather than the site centroid, those stations lie at or near the 500 m to 1 km band identified here. That the single-site field magnitudes exceed the fleet-average satellite estimate is expected: an instrumented high-impact campus sits in the upper tail of the effect distribution, whereas the ATT averages across 46 facilities of widely varying size, cooling technology, and surroundings, many of which contribute little detectable warming.

This spatial pattern is consistent with findings in the contemporaneous literature. Jing (2026) documents that daytime Landsat signals near Japanese datacenters primarily reflect albedo and land-cover changes rather than waste heat, with no detectable nighttime thermal signal. Chakraborty et al. (2026) attribute most of the measured warming to vegetation loss. If the thermal signal is primarily a land-cover rather than waste heat effect, the non-monotonic spatial pattern is expected: the facility footprint (b0) has complete impervious cover but also engineered surfaces, while the buffer zone (b1) has maximum land-cover disruption relative to pre-construction vegetation.

5.3. Economic impact

The thermal estimate is translated into implied residential cooling expenditures at the site level through a five-step conversion chain. First, daytime clear-sky LST anomalies are converted to air-temperature equivalents using a base ratio of 0.68 (Sailor et al. 2026; Benali et al. 2012; Good et al. 2017), with 0.40 and 0.90 bounds examined in a scenario analysis; regression-based LST-to-air conversions of this form are standard in the remote sensing literature, with coefficients conditioned on season and land cover (Mostovoy et al. 2006). Second, because the daytime LST anomaly need not persist over a full 24-hour cycle, a temporal persistence fraction (base: 0.68, with 0.40 and 0.90 bounds) scales the anomaly to an effective daily average, following Sailor et al. (2026) who document partial nighttime persistence at datacenter sites; the day-night distinction matters because daytime LST-air gaps vary systematically with surface conditions while nighttime LST tracks air temperature closely (Vancutsem et al. 2010). Third, the air-temperature increase is translated into additional cooling energy demand using a cooling-energy elasticity of 5 percent per degree Celsius (Auffhammer and Mansur 2014), within the 0.5 to 8.5 percent per degree range documented across building-level studies (Santamouris et al. 2015) and consistent with the cooling-driven slope of aggregate demand above comfort thresholds (Wenz et al. 2017). Fourth, additional cooling energy is valued at site-specific state residential electricity rates from the EIA (2024). Fifth, per-household costs are multiplied by GHSL-derived household counts within each distance band.

Table 5 reports the implied expenditure estimates by distance band. Uncertainty in the thermal estimates is propagated through a parametric bootstrap (5,000 draws of the band-level ATTs at their estimated means and standard errors); the resulting interval is conditional on holding the conversion ratio and persistence fraction at their baseline values, and does not incorporate uncertainty in those parameters, which the scenario grid addresses separately. Across the 46 externally dated sites, the total annual implied cooling expenditure is $0.50 million (conditional 95% CI [$0.10, $0.90]), with a mean of $10,929 per site (median $7,463). The per-household cost at 500 m to 1 km is $8.03, declining to $2.38 at 2 to 5 km. Figure 4 displays the site-level distribution, which is right-skewed: a small number of sites near dense residential areas account for a disproportionate share of the aggregate.

The bulk of the aggregate expenditure originates in the 2 to 5 km band, where household density is highest despite the attenuated thermal effect (a median of one household at 0 to 500 m versus 2,546 at 2 to 5 km). This finding implies that the extensive margin of exposure (many households experiencing a modest temperature increase) dominates the intensive margin (few households experiencing a large increase), with implications for buffer zone design.

Table 6 reports the joint scenario grid over the LST-to-air conversion ratio and the temporal persistence fraction. Varying the conversion ratio alone (at base persistence of 0.68), the sample-wide annual implied cost ranges from $0.30 million (ratio = 0.40) to $0.67 million (ratio = 0.90). The full joint grid over both parameters bounds the estimate between $0.17 million (low conversion, low persistence) and $0.88 million (high conversion, high persistence).

For the 7 treated sites with credible capacity data (1,206 MW in total; zero-valued capacity entries in the source databases are treated as missing), the implied cooling expenditure normalizes to approximately $52 per MW of capacity per year. For scale, one MW operated continuously for a year consumes 8,760 MWh, worth roughly $613,000 at a $70/MWh wholesale price, so the residential cooling channel amounts to about 0.008 percent of the facility's electricity input cost. The capacity subsample is small and skewed toward recently announced facilities, so this per-MW figure is indicative rather than representative.

The estimate is a partial accounting measure, not a lower bound: it captures only the residential cooling-energy channel and excludes health costs of heat exposure (Deschenes and Greenstone 2011; Carleton et al. 2022), property value effects (Davis 2011), and agricultural productivity losses, while itself depending on uncertain conversion, persistence, cooling consumption, and adaptation parameters that could move the estimate in either direction.

Table 4. Callaway and Sant'Anna (2021) staggered difference-in-differences estimates of spatially differenced LST.

Specification	ATT (K)	SE	95% CI	Treated sites
Panel A: Main estimates				
Post-treatment ATT (0-500 m)	+0.376	0.195	[-0.01, 0.76]	46
Pre-treatment ATT	-0.247	0.227	[-0.69, 0.20]	46
Panel B: Spatial decay				
0 to 500 m	+0.376	0.195	[-0.01, 0.76]	46
500 m to 1 km	+0.796	0.186	[0.43, 1.16]	46
1 to 2 km	+0.579	0.174	[0.24, 0.92]	46
2 to 5 km	+0.236	0.113	[0.02, 0.46]	46

Notes: Dependent variable is de-seasonalized, spatially differenced Landsat LST (inner band minus 5-10 km reference ring, in K). Treatment onset dated from VIIRS nighttime radiance threshold crossing (5 nW/cm²/sr sustained for 6+ months). Pre-existing sites excluded. Control group: not-yet-treated and never-treated sites. Sample: 46 treated sites across 9 cohorts (2016 to 2025), 13 control sites.

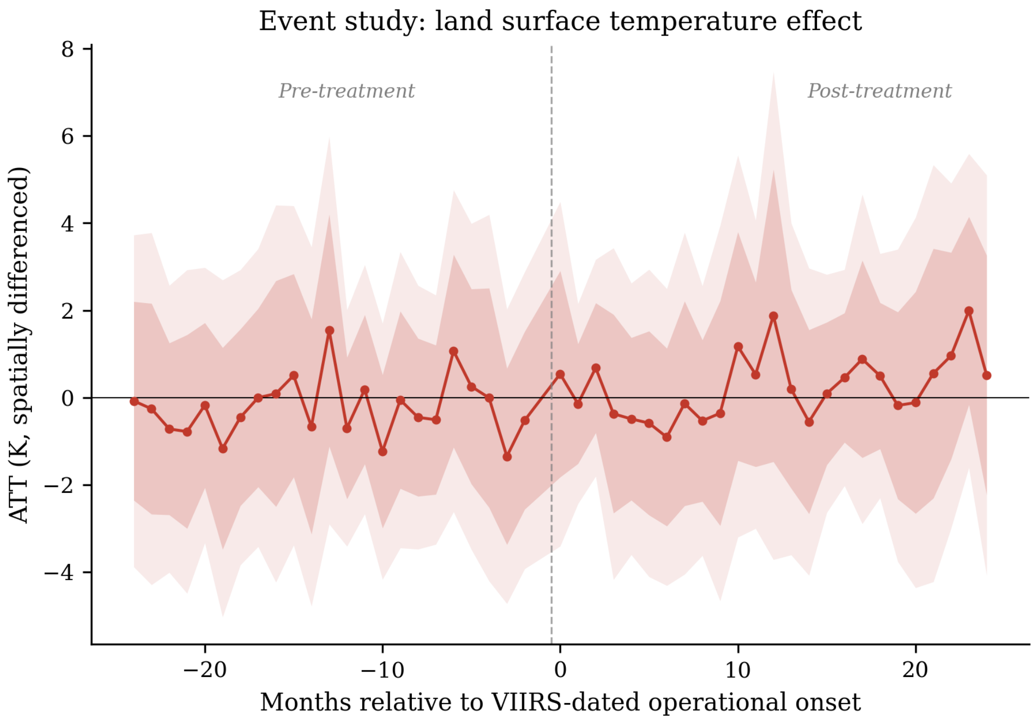

Figure 2. Event study: ATT by relative month. Dark band: pointwise 95% confidence intervals; light band: simultaneous (sup-t) 95% bands. Dashed line marks treatment onset.

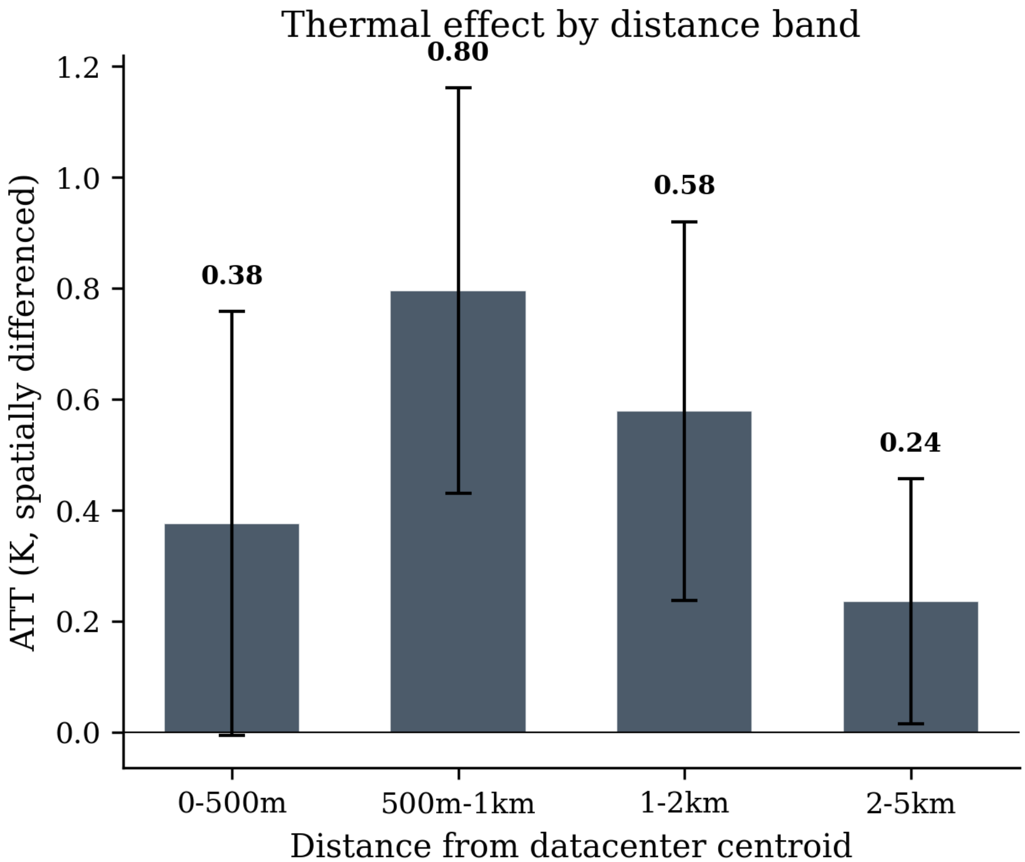

Figure 3. Spatial decay of thermal effect by distance band. Error bars show 95% confidence intervals.

Table 5. Annual implied residential cooling expenditures by distance band.

Band	ATT (K)	Mean households	$/household/yr	Total expenditure
0-500 m	+0.376	12	$3.79	$1,857
500 m-1 km	+0.796	47	$8.03	$15,965
1-2 km	+0.579	235	$5.84	$64,334
2-5 km	+0.236	3772	$2.38	$420,583
Total				$502,740

Notes: 5,000 parametric bootstrap draws of the band-level ATT estimates (normal draws at the estimated mean and standard error, propagated through the conversion chain). Sample-wide conditional 95% CI: [$100,781, $901,696], conditional on the baseline LST-to-air ratio (0.68) and persistence fraction (0.68). Cooling-energy elasticity 5%/K (Auffhammer and Mansur 2014). Residential consumption 3,100 kWh (EIA Residential Energy Consumption Survey (RECS), 2020).

Table 6. Joint scenario grid: sample-wide implied annual cooling expenditure under alternative LST-to-air conversion ratios and temporal persistence fractions.

Persistence fraction	Conversion ratio 0.40	Conversion ratio 0.68	Conversion ratio 0.90
0.40	$173,958	$295,729	$391,406
0.68	$295,729	$502,740	$665,391
0.90	$391,406	$665,391	$880,664

Notes: Cell values are the sample-wide implied annual expenditure across the 46 externally dated treated sites. The base case (0.68, 0.68) is the central estimate; all other parameters held at base values.

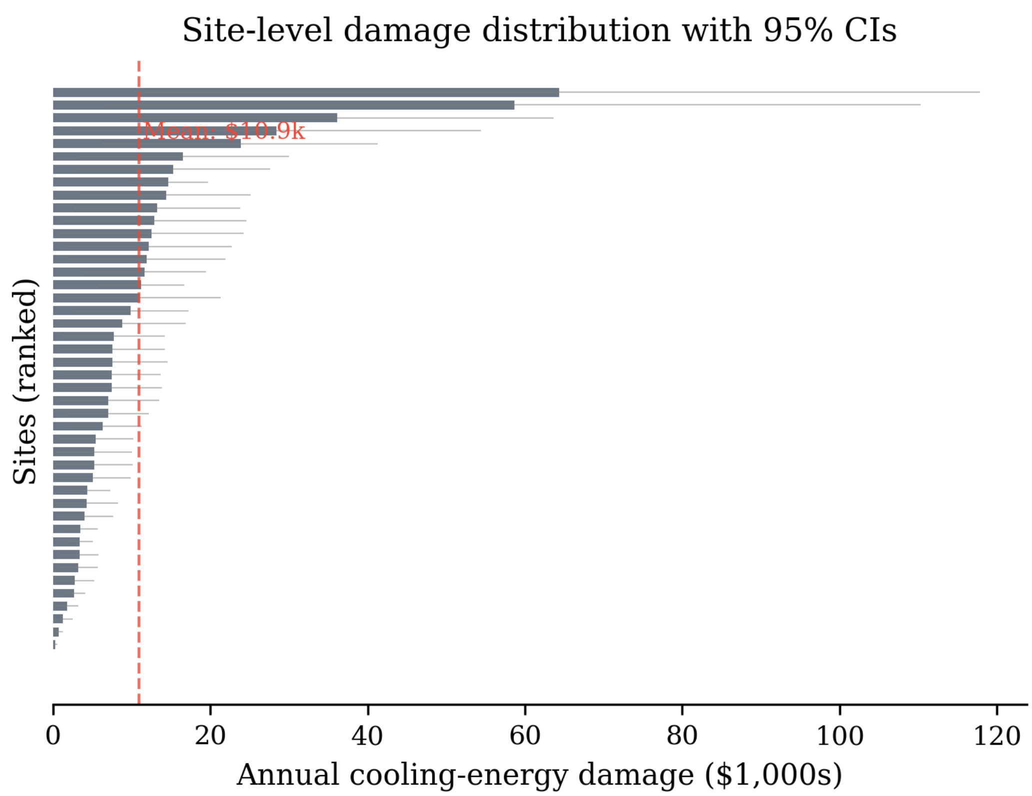

Figure 4. Site-level annual implied cooling expenditure distribution (N = 46). Dashed line shows mean ($10,929).

6. Robustness and sensitivity

Table 7 summarizes the robustness checks. Six categories of sensitivity analysis are conducted: alternative VIIRS detection thresholds, leave-one-cohort-out stability, seasonal subsamples, alternative reference ring choice, exclusion of high-capacity sites, and reference-ring independence checks.

6.1. Alternative VIIRS thresholds

The baseline VIIRS detection threshold of 5 nW/cm²/sr is varied to 3, 7, and 10 nW/cm²/sr. The thermal estimates move with the threshold, and the commissioning-date validation in Section 4.2 explains why: alternative thresholds misdate treatment. The 3 nW threshold produces a negative estimate (-2.18 K); at this threshold the validation records six undatable facilities and seven premature detections among the 17 documented commissioning dates, because rural ambient radiance is classified as operational (212 of 262 sites excluded as pre-existing, 32 retained as treated). At 7 nW, the ATT is +0.31 K ($p < 0.10$), and at 10 nW it is +0.68 K ($p < 0.01$); the validation records mean absolute dating errors of 14.5 and 26.7 months at these thresholds, as radiance accumulates gradually after energization. The threshold with by far the most accurate external dating (mean absolute error 0.9 months) is the baseline 5 nW, fixed on validation grounds in Section 4.2.

6.2. Leave-one-cohort-out

Dropping each of the 9 annual cohorts in turn produces ATT estimates ranging from 0.02 to 0.92 K. The sign is stable: the estimate is positive in all specifications. Magnitude and precision are not: the estimate is significant at the 5 percent level in 4 of 9 specifications. The largest positive shift occurs when the 2024 cohort is dropped, and the largest attenuation when the 2016 cohort is dropped, indicating meaningful heterogeneity in treatment effects across cohorts.

6.3. Seasonal splits

The summer-only (June through September) ATT is +0.85 K ($p < 0.05$), and the winter-only (December through February) ATT is +0.61 K ($p < 0.10$). The stronger summer effect is consistent with a cooling-energy mechanism: datacenter heat loads are approximately constant year-round (computational demand is not seasonal), but the ambient temperature baseline against which thermal effects are measured is higher in summer, amplifying the measured surface temperature anomaly. The seasonality is also consistent with land-cover channels (vegetation contrast is greatest in summer).

6.4. Alternative reference ring

Substituting the 2 to 5 km ring (b3) for the 5 to 10 km ring (b4) as the reference produces a positive but insignificant estimate of +0.23 K ($t = 1.40$). The attenuation is expected: the b3 ring is itself partially treated (ATT = +0.24 K in the main results), so differencing against a treated ring removes part of the signal. The 5 to 10 km reference ring remains the preferred choice, although its own untreated status is an assumption examined further in Section 6.6.

6.5. Excluding large sites

Dropping the 4 treated sites with power capacity exceeding 100 MW attenuates the ATT to +0.11 K ($t = 0.54$), a statistically insignificant estimate. The attenuation is consistent with larger facilities producing stronger thermal effects, but the small remaining sample does not permit a significant estimate without them, so the aggregate result should not be read as independent of the largest facilities.

6.6. Reference-ring independence

The spatially differenced design mechanically anchors the 5 to 10 km ring at zero, so the ring's own untreated status cannot be verified from outcomes defined relative to it. Four checks probe this assumption. First, a census of the full hyperscale universe shows that 32 of the 59 sample sites have at least one other hyperscale facility within 10 km, meaning their reference rings may contain another facility's thermal footprint; 10 sites sit in cluster markets with three or more other facilities within 20 km. Second, excluding the cluster-market sites strengthens the estimate to +0.59 K (t = 2.68, 36 treated sites), consistent with contaminated reference rings biasing the baseline toward zero rather than away from it. Third, restricting to the 16 treated sites with no other facility within 10 km leaves too few controls for stable group-time estimation; a simple pre-post comparison of the inner-versus-outer gradient in this subsample gives a mean change of +0.29 K (SE 0.29), directionally consistent with the baseline but imprecise.

Fourth, newly extracted 10 to 20 km (b5) and 20 to 30 km (b6) rings permit direct tests. Substituting these as references attenuates the 0 to 500 m estimate to +0.14 K (t = 0.63) against the 10 to 20 km ring and to approximately zero against the 20 to 30 km ring, with standard errors growing as ring area and land-use heterogeneity increase. A group-time ring test, treating the 5 to 10 km ring as the outcome differenced against the 10 to 20 km ring, is negative (-0.46 K, t = -3.73); this is the opposite sign of thermal contamination of the reference ring by the facility. The site-level version of the same test, which isolates movement at the treated sites themselves, is +0.02 K (SE 0.10, p = 0.86): the treated sites' 5 to 10 km ring does not respond to energization, and the negative group-time estimate instead reflects differential wide-ring dynamics at not-yet-treated control sites. Taken together, the checks support the untreated status of the 5 to 10 km ring at treated sites while showing that the thermal effect is not detectable against references beyond 10 km, where land-use dynamics unrelated to the facility dominate the comparison. The estimand should accordingly be read as the thermal gradient within the 10 km neighborhood of each site, not as warming relative to the broader region.

Table 7. Robustness checks. Baseline ATT: +0.376 K (SE = 0.195).

Specification	ATT (K)	SE	95% CI	
VIIRS threshold = 3 nW	-2.185	0.294	[-2.76, -1.61]	***
VIIRS threshold = 7 nW	+0.308	0.169	[-0.02, 0.64]	*
VIIRS threshold = 10 nW	+0.684	0.127	[0.44, 0.93]	***
Drop 2016 cohort (n=6)	+0.023	0.215	[-0.40, 0.45]	
Drop 2017 cohort (n=6)	+0.180	0.215	[-0.24, 0.60]	
Drop 2018 cohort (n=4)	+0.243	0.188	[-0.12, 0.61]	
Drop 2019 cohort (n=3)	+0.297	0.194	[-0.08, 0.68]	
Drop 2020 cohort (n=5)	+0.801	0.213	[0.38, 1.22]	***
Drop 2021 cohort (n=4)	+0.385	0.194	[0.01, 0.76]	**
Drop 2022 cohort (n=4)	+0.135	0.224	[-0.31, 0.57]	
Drop 2024 cohort (n=7)	+0.915	0.212	[0.50, 1.33]	***
Drop 2025 cohort (n=7)	+0.545	0.197	[0.16, 0.93]	***
Summer only (Jun-Sep)	+0.849	0.384	[0.10, 1.60]	**
Winter only (Dec-Feb)	+0.613	0.340	[-0.05, 1.28]	*
Ref ring = 2-5 km (b3)	+0.228	0.163	[-0.09, 0.55]	
Drop >100 MW sites (n=4)	+0.109	0.199	[-0.28, 0.50]	

Excl. cluster markets (3+ sites in 20 km)	+0.586	0.219	[0.16, 1.02]	***
Reference ring = 10-20 km (b5)	+0.140	0.224	[-0.30, 0.58]	
Reference ring = 20-30 km (b6)	-0.017	0.279	[-0.56, 0.53]	
Ring test: 5-10 km vs 10-20 km	-0.464	0.124	[-0.71, -0.22]	***

*Notes: *** $p < 0.01$, ** $p < 0.05$, * $p < 0.10$. Each row re-estimates the overall post-treatment ATT under alternative specifications. See Section 6 for details.*

7. Discussion and conclusion

7.1. Interpretation

The estimated thermal effect of +0.38 K in spatially differenced LST is smaller than the correlational magnitudes in the emerging literature: Marinoni et al. (2026) report +2.07 K using global cross-sections, and Chakraborty et al. (2026) find +1.44 K in summer. The attenuation is consistent with site-selection confounding in cross-sectional designs: datacenter operators select sites on characteristics (prior land clearing, low vegetation, proximity to roads and power lines) that also elevate local temperature relative to surrounding rural land, inflating spatial comparisons.

The estimand deserves precise statement. What is identified is the change in the local daytime surface-temperature gradient, within the 10 km neighborhood of each site, following VIIRS-detected facility energization. It may reflect operational ramp-up, continuing site development, and correlated land-cover changes around the energization date, but it does not identify the complete effect of converting greenfield land into a datacenter campus: much of the land clearing and impervious-surface construction occurs before VIIRS detects energization and is differenced out by the pre-treatment baseline. The composite estimated here is accordingly an incremental change around energization, and a conservative measure of the total development effect.

Within that incremental change, the daytime LST signal reflects a composite of channels: waste heat dissipation from cooling systems, albedo changes from replacing vegetation with impervious surfaces, and reduced evapotranspiration (Jing 2026; Chakraborty et al. 2026). The non-monotonic spatial decay pattern (b1 > b0) and the seasonal heterogeneity (summer > winter) are both consistent with a land-cover-dominated signal. Future work pairing daytime Landsat LST with nighttime VIIRS thermal data could separate the waste heat and land-cover channels more precisely.

7.2. Policy implications

The economically salient finding is that the thermal effect is detectable but the residential cooling-expenditure channel is modest relative to facility scale, and concentrated in a small number of densely populated sites. The largest per-household burden is $8.03 annually in the 500 m to 1 km zone, the mean facility-level implied cost is $10,929 per year, and the capacity-normalized figure is roughly $52 per MW-year, a small fraction of facility operating costs. These magnitudes favor targeted responses over broad restrictions: site-specific mitigation at the minority of facilities with substantial nearby populations, rather than siting moratoria applied to all development.

The magnitudes also bear on how datacenter siting fits the broader local-externality template. The hedonic literature finds that proximate energy infrastructure is capitalized into house prices at magnitudes of several percent within 2 km (Gibbons 2015; Droes and Koster 2016; Davis 2011), and welfare accounting for host communities weighs such amenity costs against employment and tax-base gains (Bartik et al. 2019; Alvarez et al. 2026). A cooling-expenditure burden of $8.03 per household per year is at least an order of magnitude too small to generate hedonic effects of that size on its own. The property value and amenity concerns voiced in siting disputes therefore rest primarily on channels other than thermal cooling costs: noise, viewshed, water, and land use. By implication, blocking projects on thermal grounds alone carries the opposition costs documented for other energy infrastructure (Jarvis 2025) with little offsetting benefit through the cooling-cost channel measured here.

Two targeted instruments follow from the spatial pattern. The decay gradient peaks in the 500 m to 1 km band, so setback or buffer arrangements between campuses and residential areas, analogous to setback requirements for power plants and industrial facilities (Currie et al. 2015), would capture the zone of maximum impact where they are warranted at all; whether they pass a benefit-cost test depends on land costs that this paper does not estimate. In addition, if the thermal signal is primarily driven by land-cover change rather than waste heat, as suggested by Jing (2026), then vegetated buffers, permeable surfaces, and green infrastructure may be more effective and less costly than engineering solutions focused on heat rejection systems; several operators have already adopted campus vegetation requirements (Google 2023; Microsoft 2024).

A final implication concerns the energy system rather than the neighborhood. The local cooling demand induced by datacenter warming adds to residential load in summer afternoons, precisely when warming raises peak system load (Auffhammer et al. 2017), so the thermal channel compounds, marginally, the grid stress that datacenter electricity demand itself creates. Against this, the spatial flexibility of computational load gives datacenters a compensating role as grid resources (Zheng et al. 2020), and the per-MW magnitude estimated here implies the induced-cooling component is negligible relative to the facility's own load: the siting question, not the system operation question, is where the thermal externality binds.

7.3. Limitations

Several limitations qualify these findings. The sample of 46 externally dated treated sites and 13 never-treated controls across 9 cohorts is small, driven by the stringent exclusion of pre-existing and early-treated sites. The headline 0 to 500 m estimate is significant only at the 10 percent level, and the small number of treated units limits the precision of heterogeneity analyses (by capacity class, climate zone, or cooling technology); the strongest statistical evidence lies in the 500 m to 2 km bands. The wider-ring checks in Section 6.6 bound the claim spatially: the effect is identified as a gradient within the 10 km neighborhood and is not detectable against references beyond 10 km.

The economic calculation is a partial accounting measure restricted to the residential cooling-energy channel. Health costs of heat exposure, including excess mortality (Deschenes and Greenstone 2011; Carleton et al. 2022), morbidity (Barreca et al. 2016), and labor productivity losses (Graff Zivin and Neidell 2014), are excluded, as are property value effects (Davis 2011) and agricultural productivity losses. At the same time, the included channel itself depends on uncertain conversion, persistence, consumption, and adaptation parameters, so the estimate should not be described as a bound in either direction. The calculation also ignores the feedback from air-conditioning use itself, which adds anthropogenic heat to the local environment (Salamanca et al. 2014) and would amplify the thermal anomaly slightly beyond the direct facility effect.

The LST-to-air-temperature conversion ratio (0.68) and the temporal persistence fraction (0.68) are the most uncertain parameters in the conversion chain. The joint scenario analysis over both parameters bounds the sample-wide implied cost between \$0.17 and \$0.88 million annually. Field validation pairing satellite-derived LST with ground-station air-temperature measurements at datacenter sites would reduce this uncertainty.

7.4. Conclusion

Hyperscale datacenter energization is associated with a measurable increase in the local land-surface temperature gradient. Using externally dated treatment timing from VIIRS nighttime radiance, validated against documented commissioning dates, and a spatially differenced outcome design, the estimated change peaks at +0.80 K in the 500 m to 1 km band, with +0.38 K within 500 m and +0.24 K at 2 to 5 km. The sign is stable across leave-one-cohort-out specifications and seasonal subsamples, and the estimate strengthens when cluster markets with potentially contaminated reference rings are excluded, although magnitude and precision vary across specifications. Translating this thermal footprint into residential cooling costs implies annual expenditures of \$0.50 million across 46 operational sites, roughly \$52 per MW-year in the subsample with documented capacity: a detectable but modest externality channel, concentrated where facilities adjoin dense residential areas, providing an empirical anchor for the infrastructure siting debate surrounding datacenter development.

Declaration of generative AI and AI-assisted technologies in the manuscript preparation process

During the preparation of this work, the authors used Claude (Anthropic) to program and debug some of the Python scripts that downloaded, stored and processed data. The author take full responsibility for the content of the published article.

References

Akbari, H., Pomerantz, M., and Taha, H. (2001). Cool surfaces and shade trees to reduce energy use and improve air quality in urban areas. Solar Energy, 70(3), 295-310. https://doi.org/10.1016/S0038-092X(00)00089-X

Alvarez, F., Argente, D., Chow, J., and Van Patten, D. (2026). Data centers and local economies in the age of AI: A shift-share approach. NBER Working Paper 35194. https://doi.org/10.3386/w35194

An Bord Pleanala (2022). Decision on datacenter planning applications in South Dublin County. Dublin, Ireland: An Bord Pleanala.

Arnfield, A.J. (2003). Two decades of urban climate research: A review of turbulence, exchanges of energy and water, and the urban heat island. International Journal of Climatology, 23(1), 1-26. https://doi.org/10.1002/joc.859

Auffhammer, M. and Mansur, E.T. (2014). Measuring climatic impacts on energy consumption: A review of the empirical literature. Energy Economics, 46, 522-530. https://doi.org/10.1016/j.eneco.2014.04.017

Auffhammer, M., Baylis, P., and Hausman, C.H. (2017). Climate change is projected to have severe impacts on the frequency and intensity of peak electricity demand across the United States. Proceedings of the National Academy of Sciences, 114(8), 1886-1891. https://doi.org/10.1073/pnas.1613193114

Baker, A.C., Larcker, D.F., and Wang, C.C.Y. (2022). How much should we trust staggered difference-in-differences estimates? Journal of Financial Economics, 144(2), 370-395. https://doi.org/10.1016/j.jfineco.2022.01.004

Barreca, A., Clay, K., Deschenes, O., Greenstone, M., and Shapiro, J.S. (2016). Adapting to climate change: The remarkable decline in the US temperature-mortality relationship over the twentieth century. Journal of Political Economy, 124(1), 105-159. https://doi.org/10.1086/684582

Bartik, A.W., Currie, J., Greenstone, M., and Knittel, C.R. (2019). The local economic and welfare consequences of hydraulic fracturing. American Economic Journal: Applied Economics, 11(4), 105-155. https://doi.org/10.1257/app.20170487

Benali, A., Carvalho, A.C., Nunes, J.P., Carvalhais, N., and Santos, A. (2012). Estimating air surface temperature in Portugal using MODIS LST data. Remote Sensing of Environment, 124, 108-121. https://doi.org/10.1016/j.rse.2012.04.024

Borusyak, K., Jaravel, X., and Spiess, J. (2024). Revisiting event-study designs: Robust and efficient estimation. Review of Economic Studies, 91(6), 3253-3285. https://doi.org/10.1093/restud/rdae007

Callaway, B. and Sant'Anna, P.H.C. (2021). Difference-in-differences with multiple time periods. Journal of Econometrics, 225(2), 200-230. https://doi.org/10.1016/j.jeconom.2020.12.001

Cameron, A.C., Gelbach, J.B., and Miller, D.L. (2008). Bootstrap-based improvements for inference with clustered errors. The Review of Economics and Statistics, 90(3), 414-427. https://doi.org/10.1162/rest.90.3.414

Carleton, T., Jina, A., Delgado, M., Greenstone, M., Houser, T., Hsiang, S., Hultgren, A., Kopp, R.E., McCusker, K.E., Nath, I., Rising, J., Rode, A., Seo, H.K., Viaene, A., Yuan, J., and Zhang, A.T. (2022). Valuing the global mortality consequences of climate change accounting for adaptation costs and benefits. Quarterly Journal of Economics, 137(4), 2037-2105. https://doi.org/10.1093/qje/qjac020

Chakraborty, T., Venter, Z.S., Qian, Y., and Lee, X. (2026). Thermal impacts of data centers on local land surface temperature. EarthArXiv Preprint 13215. https://doi.org/10.31223/X5TM7Q

Clinton, N. and Gong, P. (2013). MODIS detected surface urban heat islands and sinks: Global locations and controls. Remote Sensing of Environment, 134, 294-304. https://doi.org/10.1016/j.rse.2013.03.008

Conley, T.G. and Taber, C.R. (2011). Inference with "Difference in Differences" with a small number of policy changes. The Review of Economics and Statistics, 93(1), 113-125. https://doi.org/10.1162/REST_a_00049

Currie, J., Davis, L., Greenstone, M., and Walker, R. (2015). Environmental health risks and housing values: Evidence from 1,600 toxic plant openings and closings. American Economic Review, 105(2), 678-709. https://doi.org/10.1257/aer.20110185

Davis, L.W. (2011). The effect of power plants on local housing values and rents. The Review of Economics and Statistics, 93(4), 1391-1402. https://doi.org/10.1162/REST_a_00119

Davis, L.W. and Gertler, P.J. (2015). Contribution of air conditioning adoption to future energy use under global warming. Proceedings of the National Academy of Sciences, 112(19), 5962-5967. https://doi.org/10.1073/pnas.1423558112

de Chaisemartin, C. and D'Haultfoeuille, X. (2020). Two-way fixed effects estimators with heterogeneous treatment effects. American Economic Review, 110(9), 2964-2996. https://doi.org/10.1257/aer.20181169

Depoorter, V., Oro, E., and Salom, J. (2015). The location as an energy efficiency and renewable energy supply measure for data centres in Europe. Applied Energy, 140, 338-349. https://doi.org/10.1016/j.apenergy.2014.11.067

de Vries, A. (2023). The growing energy footprint of artificial intelligence. Joule, 7(10), 2191-2194. https://doi.org/10.1016/j.joule.2023.09.004

Deschenes, O. and Greenstone, M. (2011). Climate change, mortality, and adaptation: Evidence from annual fluctuations in weather in the US. American Economic Journal: Applied Economics, 3(4), 152-185. https://doi.org/10.1257/app.3.4.152

Deschenes, O. and Moretti, E. (2009). Extreme weather events, mortality, and migration. Review of Economics and Statistics, 91(4), 659-681. https://doi.org/10.1162/rest.91.4.659

Donaldson, D. and Storeygard, A. (2016). The view from above: Applications of satellite data in economics. Journal of Economic Perspectives, 30(4), 171-198. https://doi.org/10.1257/jep.30.4.171

Droes, M.I. and Koster, H.R.A. (2016). Renewable energy and negative externalities: The effect of wind turbines on house prices. Journal of Urban Economics, 96, 121-141. https://doi.org/10.1016/j.jue.2016.09.001

Energy Information Administration (2020). 2020 Residential Energy Consumption Survey (RECS). Washington, DC: US Department of Energy. https://www.eia.gov/consumption/residential/

Energy Information Administration (2024). Electric Power Monthly. Washington, DC: US Department of Energy. https://www.eia.gov/electricity/monthly/

Epoch AI (2025). Frontier Data Centers dataset. https://epoch.ai/data/frontier-data-centers

Estrada, F., Botzen, W.J.W., and Tol, R.S.J. (2017). A global economic assessment of city policies to reduce climate change impacts. Nature Climate Change, 7(6), 403-406. https://doi.org/10.1038/nclimate3301

Fang, T.P. and Greenstein, S. (2025). Where the cloud rests: The economic geography of data centers. Strategy Science, 10(4), 404-420. https://doi.org/10.1287/stsc.2024.0225

Ferman, B. and Pinto, C. (2019). Inference in differences-in-differences with few treated groups and heteroskedasticity. The Review of Economics and Statistics, 101(3), 452-467. https://doi.org/10.1162/rest_a_00759

Freyaldenhoven, S., Hansen, C., and Shapiro, J.M. (2019). Pre-event trends in the panel event-study design. American Economic Review, 109(9), 3307-3338. https://doi.org/10.1257/aer.20180609

Gibbons, S. (2015). Gone with the wind: Valuing the visual impacts of wind turbines through house prices. Journal of Environmental Economics and Management, 72, 177-196. https://doi.org/10.1016/j.jeem.2015.04.006

Good, E.J., Ghent, D.J., Bulgin, C.E., and Remedios, J.J. (2017). A spatiotemporal analysis of the relationship between near-surface air temperature and satellite land surface temperatures using 17 years of data from the ATSR series. Journal of Geophysical Research: Atmospheres, 122(17), 9185-9210. https://doi.org/10.1002/2017JD026880

Goodman-Bacon, A. (2021). Difference-in-differences with variation in treatment timing. Journal of Econometrics, 225(2), 254-277. https://doi.org/10.1016/j.jeconom.2021.03.014

Google (2023). Environmental report 2023. Mountain View, CA: Alphabet Inc.

Graff Zivin, J. and Neidell, M. (2014). Temperature and the allocation of time: Implications for climate change. Journal of Labor Economics, 32(1), 1-26. https://doi.org/10.1086/671766

Greenstone, M. and Gallagher, J. (2008). Does hazardous waste matter? Evidence from the housing market and the Superfund program. The Quarterly Journal of Economics, 123(3), 951-1003. https://doi.org/10.1162/qjec.2008.123.3.951

Henderson, J.V., Storeygard, A., and Weil, D.N. (2012). Measuring economic growth from outer space. American Economic Review, 102(2), 994-1028. https://doi.org/10.1257/aer.102.2.994

IEA (2024). Electricity 2024: Analysis and forecast to 2026. Paris: International Energy Agency. https://doi.org/10.1787/da8f6222-en

Imhoff, M.L., Zhang, P., Wolfe, R.E., and Bounoua, L. (2010). Remote sensing of the urban heat island effect across biomes in the continental USA. Remote Sensing of Environment, 114(3), 504-513. https://doi.org/10.1016/j.rse.2009.10.008

Infocomm Media Development Authority (2019). Advisory on new data centre facilities. Singapore: IMDA.

Jarvis, S. (2025). The economic costs of NIMBYism: Evidence from renewable energy projects. Journal of the Association of Environmental and Resource Economists, 12(4), 983-1022. https://doi.org/10.1086/732801

Jing, C. (2026). Quantifying local thermal effects from data centers in Japan using multi-source satellite observations. EarthArXiv Preprint 13854. https://doi.org/10.31223/X5F42K

Kollar, A. and Grady, C. (2025). U.S. Data Center Risk Repository [Data set]. Zenodo. https://doi.org/10.5281/zenodo.17372375

Koot, M. and Wijnhoven, F. (2021). Usage impact on data center electricity needs: A system dynamic forecasting model. Applied Energy, 291, 116798. https://doi.org/10.1016/j.apenergy.2021.116798

Lei, N. and Masanet, E. (2020). Statistical analysis for predicting location-specific data center PUE and its improvement potential. Energy, 201, 117556. https://doi.org/10.1016/j.energy.2020.117556

Li, X., Zhou, W., and Ouyang, Z. (2013). Relationship between land surface temperature and spatial pattern of greenspace: What are the effects of spatial resolution? Landscape and Urban Planning, 114, 1-8. https://doi.org/10.1016/j.landurbplan.2013.02.005

Loudoun County Board of Supervisors (2024). Resolution on datacenter development moratorium. Leesburg, VA: Loudoun County.

Madden, N., Lewis, A., and Davis, M. (2013). Thermal effluent from the power sector: An analysis of once-through cooling system impacts on surface water temperature. Environmental Research Letters, 8(3), 035006. https://doi.org/10.1088/1748-9326/8/3/035006

Malakar, N.K., Hulley, G.C., Hook, S.J., Laraby, K., Cook, M., and Schott, J.R. (2018). An operational land surface temperature product for Landsat thermal data: Methodology and validation. IEEE Transactions on Geoscience and Remote Sensing, 56(10), 5717-5735. https://doi.org/10.1109/TGRS.2018.2824828

Marinoni, M., Pritoni, M., and Wetter, M. (2026). Satellite assessment of the thermal footprint of data centers. arXiv Preprint 2603.20897. https://doi.org/10.48550/arXiv.2603.20897

Marx, B., Stoker, T.M., and Suri, T. (2019). There is no free house: Ethnic patronage in a Kenyan slum. American Economic Journal: Applied Economics, 11(4), 36-70. https://doi.org/10.1257/app.20160484

Masanet, E., Shehabi, A., Lei, N., Smith, S., and Koomey, J. (2020). Recalibrating global data center energy-use estimates. Science, 367(6481), 984-986. https://doi.org/10.1126/science.aba3758

Microsoft (2024). Environmental sustainability report 2024. Redmond, WA: Microsoft Corporation.

Montiel Olea, J.L. and Plagborg-Moller, M. (2019). Simultaneous confidence bands: Theory, implementation, and an application to SVARs. Journal of Applied Econometrics, 34(1), 1-17. https://doi.org/10.1002/jae.2656

Mostovoy, G.V., King, R.L., Reddy, K.R., and Kakani, V.G. (2006). Statistical estimation of daily maximum and minimum air temperatures from MODIS LST data over the state of Mississippi. GIScience and Remote Sensing, 43(1), 78-110. https://doi.org/10.2747/1548-1603.43.1.78

Muehlenbachs, L., Spiller, E., and Timmins, C. (2015). The housing market impacts of shale gas development. American Economic Review, 105(12), 3633-3659. https://doi.org/10.1257/aer.20140079

Muller, N.Z. (2026). Measuring the impact of data centers in the United States economy: Monetary damage from air pollution and greenhouse gas emissions. NBER Working Paper 35100. https://doi.org/10.3386/w35100

Mytton, D. (2021). Data centre water consumption. npj Clean Water, 4, 11. https://doi.org/10.1038/s41545-021-00101-w

Oke, T.R. (1982). The energetic basis of the urban heat island. Quarterly Journal of the Royal Meteorological Society, 108(455), 1-24. https://doi.org/10.1002/qj.49710845502

Oke, T.R., Mills, G., Christen, A., and Voogt, J.A. (2017). Urban Climates. Cambridge University Press. https://doi.org/10.1017/9781139016476

O'Neill, B.C., et al. (2022). IM3 Data Center Atlas. Richland, WA: Pacific Northwest National Laboratory.

Patterson, D., Gonzalez, J., Le, Q., Liang, C., Munguia, L.-M., Rothchild, D., So, D., Texier, M., and Dean, J. (2021). Carbon emissions and large neural network training. arXiv Preprint 2104.10350. https://doi.org/10.48550/arXiv.2104.10350

Peng, S., Piao, S., Ciais, P., Friedlingstein, P., Ottle, C., Breon, F.-M., Nan, H., Zhou, L., and Myneni, R.B. (2012). Surface urban heat island across 419 global big cities. Environmental Science and Technology, 46(2), 696-703. https://doi.org/10.1021/es2030438

Rambachan, A. and Roth, J. (2023). A more credible approach to parallel trends. The Review of Economic Studies, 90(5), 2555-2591. https://doi.org/10.1093/restud/rdad018

Ristic, B., Madani, K., and Makuch, Z. (2015). The water footprint of data centers. Sustainability, 7(8), 11260-11284. https://doi.org/10.3390/su70811260

Roth, J. (2022). Pretest with caution: Event-study estimates after testing for parallel trends. American Economic Review: Insights, 4(3), 305-322. https://doi.org/10.1257/aeri.20210236

Roth, J., Sant'Anna, P.H.C., Bilinski, A., and Poe, J. (2023). What's trending in difference-in-differences? A synthesis of the recent econometrics literature. Journal of Econometrics, 235(2), 2218-2244. https://doi.org/10.1016/j.jeconom.2023.03.008

Sailor, D.J., Samareh Abolhassani, S., and Martin, E.P. (2026). Data center waste heat as an emerging urban thermal hazard: First field measurements of neighborhood-scale air temperature impacts. ASME Journal of Engineering for Sustainable Buildings and Cities, 7(2), 024501. https://doi.org/10.1115/1.4071922

Salamanca, F., Georgescu, M., Mahalov, A., Moustaoui, M., and Wang, M. (2014). Anthropogenic heating of the urban environment due to air conditioning. Journal of Geophysical Research: Atmospheres, 119(10), 5949-5965. https://doi.org/10.1002/2013JD021225

Santamouris, M., Cartalis, C., Synnefa, A., and Kolokotsa, D. (2015). On the impact of urban heat island and global warming on the power demand and electricity consumption of buildings: A review. Energy and Buildings, 98, 119-124. https://doi.org/10.1016/j.enbuild.2014.09.052

Shehabi, A., Smith, S.J., Sartor, D.A., Brown, R.E., Herrlin, M., Koomey, J.G., Masanet, E.R., Horner, N., Azevedo, I.L., and Lintner, W. (2016). United States Data Center Energy Usage Report. LBNL-1005775. Berkeley, CA: Lawrence Berkeley National Laboratory. https://doi.org/10.2172/1372902

Siddik, M.A.B., Shehabi, A., and Marston, L. (2021). The environmental footprint of data centers in the United States. Environmental Research Letters, 16(6), 064017. https://doi.org/10.1088/1748-9326/abfba1

Stewart, I.D. and Oke, T.R. (2012). Local climate zones for urban temperature studies. Bulletin of the American Meteorological Society, 93(12), 1879-1900. https://doi.org/10.1175/BAMS-D-11-00019.1

Sun, L. and Abraham, S. (2021). Estimating dynamic treatment effects in event studies with heterogeneous treatment effects. Journal of Econometrics, 225(2), 175-199. https://doi.org/10.1016/j.jeconom.2020.09.006

Synergy Research Group (2025). Hyperscale data center investment tracker: 2024 year-end report. Reno, NV: Synergy Research Group.

US Census Bureau (2020). 2020 Census: Average Household Size. Washington, DC: US Department of Commerce. https://data.census.gov/

Vancutsem, C., Ceccato, P., Dinku, T., and Connor, S.J. (2010). Evaluation of MODIS land surface temperature data to estimate air temperature in different ecosystems over Africa. Remote Sensing of Environment, 114(2), 449-465. https://doi.org/10.1016/j.rse.2009.10.002

Voogt, J.A. and Oke, T.R. (2003). Thermal remote sensing of urban climates. Remote Sensing of Environment, 86(3), 370-384. https://doi.org/10.1016/S0034-4257(03)00079-8

Wan, Z. (2014). New refinements and validation of the collection-6 MODIS land-surface temperature/emissivity product. Remote Sensing of Environment, 140, 36-45. https://doi.org/10.1016/j.rse.2013.08.027

Wenz, L., Levermann, A., and Auffhammer, M. (2017). North-south polarization of European electricity consumption under future warming. Proceedings of the National Academy of Sciences, 114(38), E7910-E7918. https://doi.org/10.1073/pnas.1704339114

Zheng, J., Chien, A.A., and Suh, S. (2020). Mitigating curtailment and carbon emissions through load migration between data centers. Joule, 4(10), 2208-2222. https://doi.org/10.1016/j.joule.2020.08.001

Zhou, D., Zhao, S., Liu, S., Zhang, L., and Zhu, C. (2014). Surface urban heat island in China's 32 major cities: Spatial patterns and drivers. Remote Sensing of Environment, 152, 51-61. https://doi.org/10.1016/j.rse.2014.05.017